Science Advances

Supplementary Materials for

Amorphization mechanism of SrIrO₃ electrocatalyst: How oxygen redox initiates ionic diffusion and structural reorganization

Gang Wan, John W. Freeland, Jan Kloppenburg, Guido Petretto, Jocienne N. Nelson, Ding-Yuan Kuo, Cheng-Jun Sun, Jianguo Wen, J. Trey Diulus, Gregory S. Herman, Yongqi Dong, Ronghui Kou, Jingying Sun, Shuo Chen, Kyle M. Shen, Darrell G. Schlom, Gian-Marco Rignanese, Geoffroy Hautier, Dillon D. Fong*, Zhenxing Feng*, Hua Zhou*, Jin Suntivich*

*Corresponding author. Email: fong@anl.gov (D.D.F.); zhenxing.feng@oregonstate.edu (Z.F.); hzhou@aps.anl.gov (H.Z.); jsuntivich@cornell.edu (J. Suntivich)

The PDF file includes:

Sections S1 to S7
Figs. S1 to S14
Tables S1 to S3

Other Supplementary Material for this manuscript includes the following:

(available at advances.sciencemag.org/cgi/content/full/7/2/eabc7323/DC1)

Structure file for amorphous IrO₂ with 96 atoms (1)
Structure file for amorphous IrO₂ with 96 atoms (2)
Structure file for amorphous IrO₂ with 192 atoms

Section 1. Electrochemical Measurements
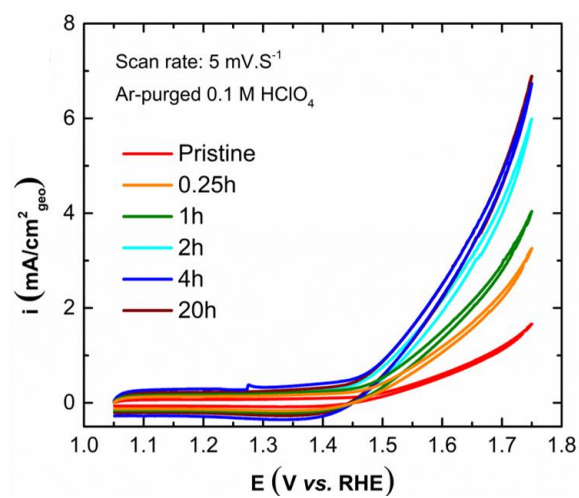
Fig. S1. Electrochemical cycling of SrIrO₃. OER of a SrIrO$_3$ film grown on DyScO$_3$ was recorded at a scan rate of 5 mV/s in 0.1 M HClO$_4$ purged with Ar. The results are shown for pristine SrIrO$_3$ film, SrIrO$_3$ after 0.25 h, 1h, and 4h of cycling.
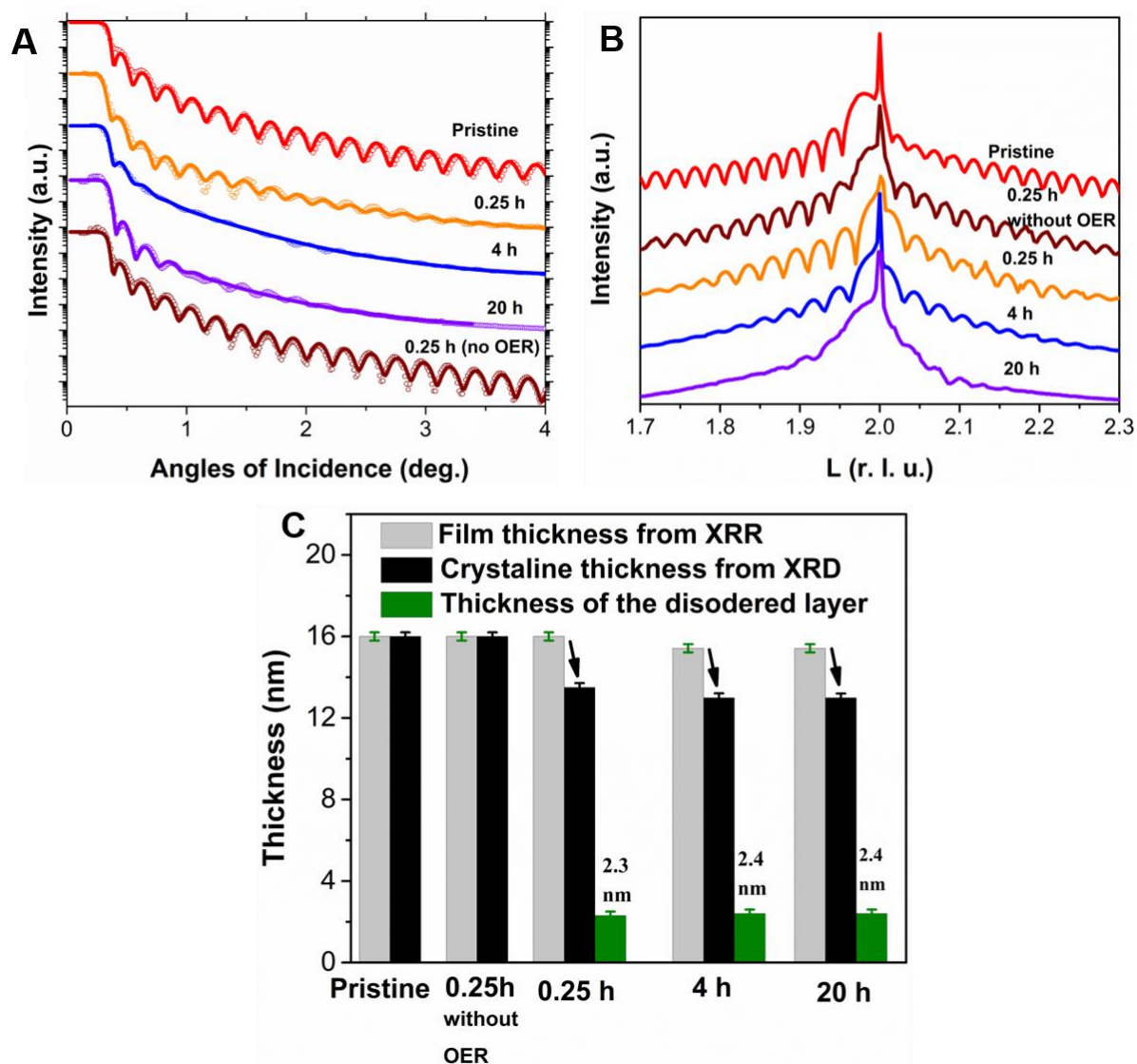
Fig. S2. XRR and XRD of the pristine and cycled SrIrO₃. (A) X-ray reflectivity (XRR, data and fitting curves, black and colored), **(B)** X-ray diffraction (XRD), and **(C)** the extracted thickness of the total film, the crystalline layer, and the amorphous layer of the the SrIrO₃ film in the pristine state and after 0.25 h, 4 h, and 20 h of potential cycling between 1.05 – 1.75 V vs. RHE, and after 0.25 h of potential cycling between 0.8 – 1 V vs. RHE.

| SrIrO₃ Conditions / Fitting Parameters	Prisitine	No OER	0.25 h	4 h	20 h
Total SrIrO$_3$ Film Thickness d_t	16.0 ± 0.1 nm	16.1 ± 0.1 nm	15.8 ± 0.4 nm	15.4 ± 0.5 nm	15.3 ± 0.5 nm
Surface SrIrO$_x$ Amorphized Layer Thickness d_a			2.3 ± 0.3 nm	2.4 ± 0.4 nm	2.4 ± 0.4 nm
Crystalline SrIrO$_{3-\delta}$ Bottom Layer Thickness d_c			13.5 ± 0.3 nm	13.0 ± 0.4 nm	12.9 ± 0.4 nm
DyScO$_3$ Substrate and Film Interfacial Roughness σ_I	0.05 ± 0.04 nm	0.11 ± 0.02 nm	0.32 ± 0.04 nm	1.50 ± 0.11 nm	1.20 ± 0.08 nm
Amorphized and Crsytalline Layer Interfacial Roughness σ_{II}			0.86 ± 0.18 nm	0.31 ± 0.25 nm	1.46 ± 0.33 nm
SrIrO$_x$ Film Surface Roguhenss σ_s	0.16 ± 0.02 nm	0.16 ± 0.01 nm	0.11 ± 0.02 nm	0.19 ± 0.01 nm	0.16 ± 0.03 nm
XRR Layer Models	One Layer	One Layer	Two Layers	Two Layers	Two Layers

Table S1. XRR experimental fitting parameters and error bars

The synchrotron-based high resolution XRR of the series of SrIrO$_3$/DyScO$_3$ films under different conditions are anlyazed and fitted by XRR fitting open source software MOTOFIT (http://motofit.sourceforge.net/, Nelson *J. Appl. Cryst.* 2006, 39, 273-276). The XRR data and fitting results is shown in Fig. S2A and Table S1 that includes the layer thickness (e.g. amorphized surface layer and crystalline bottom film layer), respective interfacial roughness and experimental errors for each fitted quantity. For simplicity, the error bar of each thickness obtained from our fitting is used in single digit precision like ± 0.X nm, and the error bar of each roughness obtained from our fitting is used in double digit precision like ± 0.XX nm. For the prisitine and no OER conditions of SrIrO$_3$, an one crystalline layer model is adopted due to the high structural integrity and smoothness without the OER induced amorphization. For the post OER conditions (including 0.25 h, 4 h and 20 h conditions), a two-layer model is adopted due to the surface amrophization and increased roughness at each interface as a result of the OER induced structural reorganization.

Section 2. XPS of pristine and cycled SrIrO₃
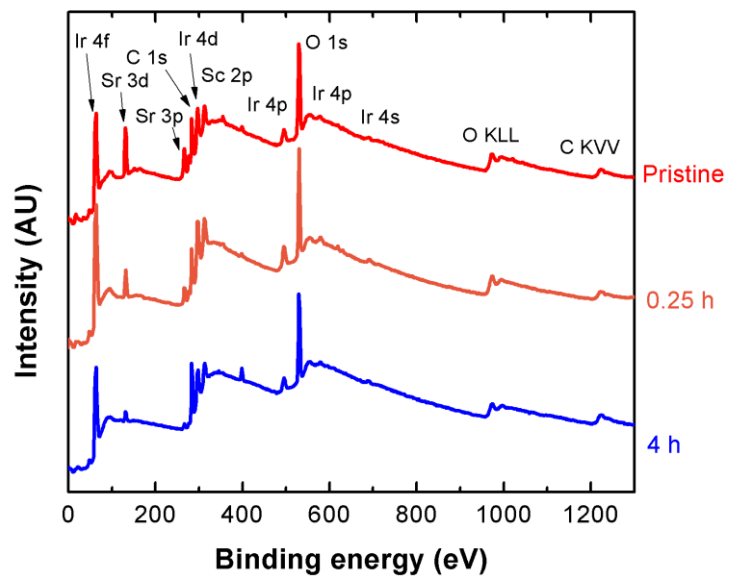
**Fig. S3. The XPS spectra of the pristine SrIrO₃ catalyst, after 0.25 h of cycling, and after 4 h of cycling.**
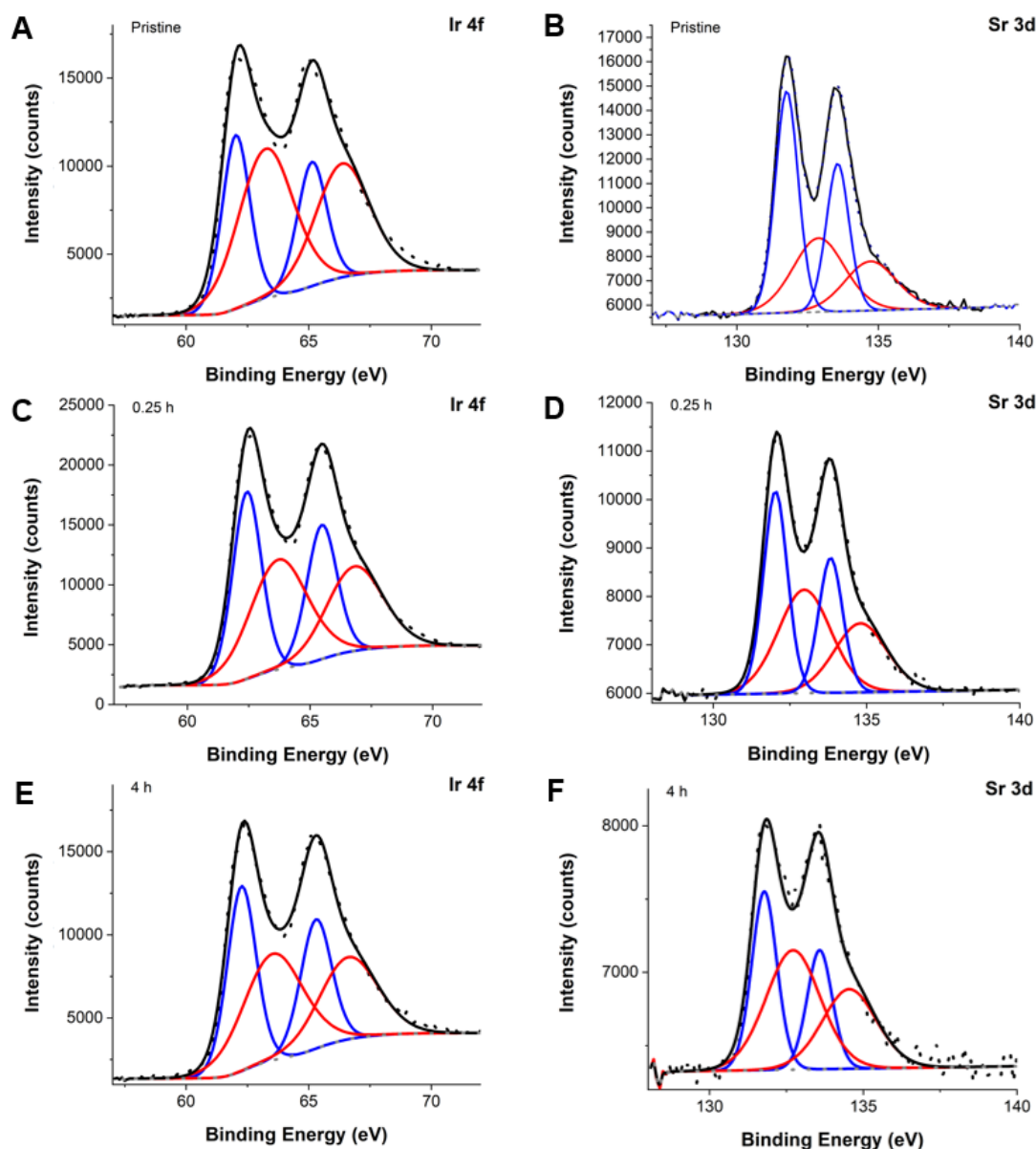
Fig. S4. The high resolution Ir 4f and Sr 3d XPS spectra of pristine SrIrO₃ catalyst (A, B), after 0.25 h of cycling (C, D), and after 4 h of cycling (E, F).

	Sr (at. %)	Ir (at. %)
Pristine	19.7 ± 0.6	19.5 ± 0.6
After 0.25 h of cycling	8.1 ± 0.3	18.4 ± 0.5
After 4 h of cycling	3.6 ± 0.2	16.5 ± 0.5

Table S2. XPS determined Sr and Ir surface compositions with experimental errors for the pristine SrIrO₃, after 0.25 h and 4 h of potential cycling.

# Section 3. Ir L$_{III}$-edge GI-XANES of pristine and cycled SrIrO$_3$
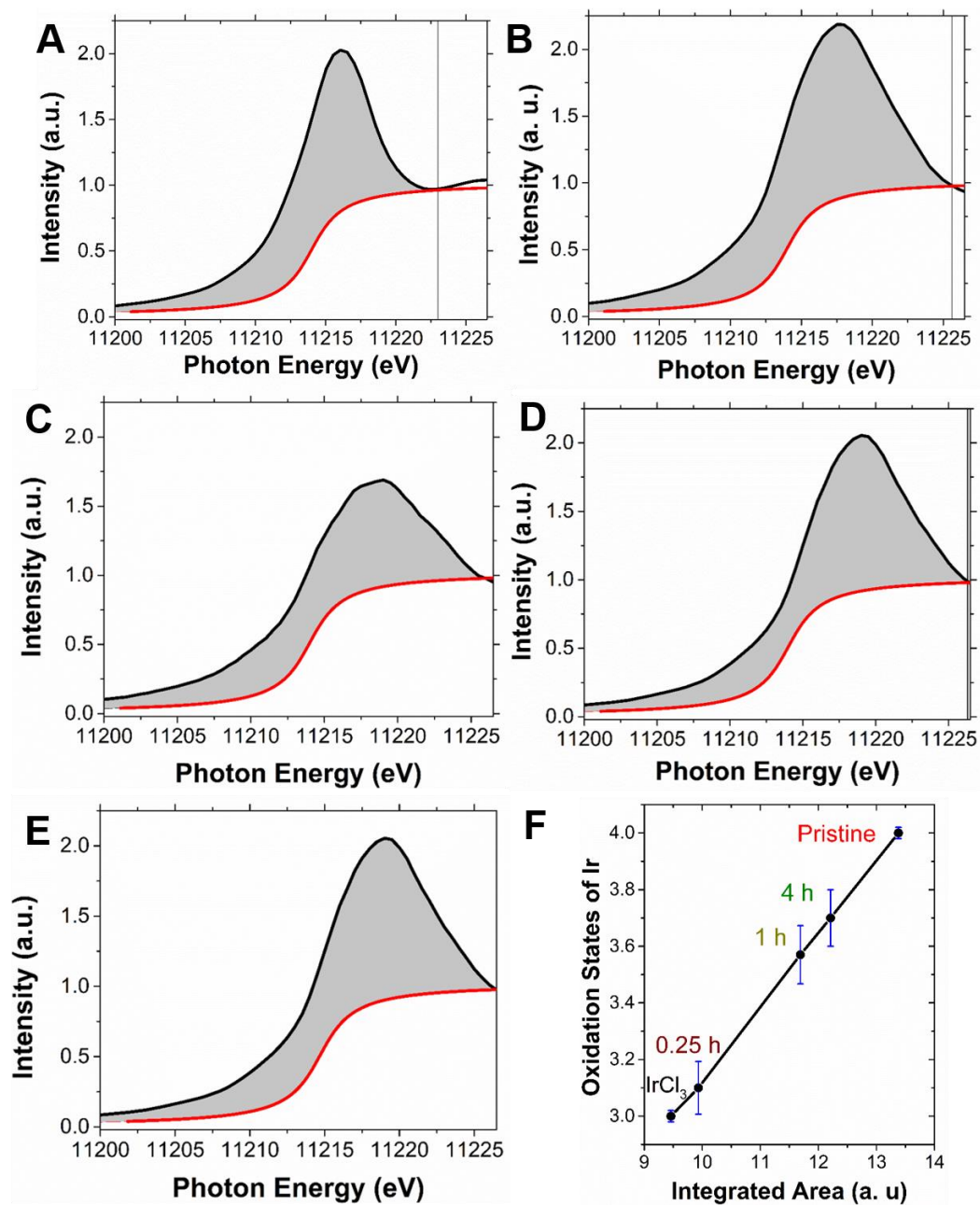
Fig. S5. Analysis of the Ir L$_{III}$-edge GI-XANES. The black lines show the experimental spectra, and the red lines show the used baseline correction for (**A**) IrCl$_3$, (**B**) pristine SrIrO$_3$, (**C**) SrIrO$_3$ after 0.25 h cycling, (**D**) 1h, and (**E**) 4h. (**F**) The formal oxidation state of Ir after different cycling times. The formal oxidation state information was determined based on the linear relationship of the integrated area (grey areas) and the oxidation states of pristine SrIrO$_3$ and IrCl$_3$ reference samples (Ir^{4+} and Ir^{3+}, respectively).
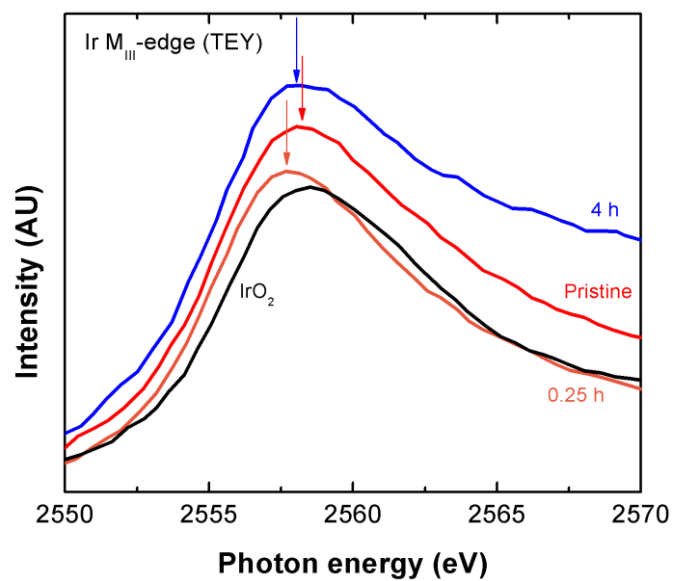
Fig. S6. The surface-sensitive Ir M$_{III}$-edge XANES of IrO$_2$, pristine SrIrO$_3$, SrIrO$_3$ after 0.25 h, 1h, and 4h of cycling in the total electron yield (TEY) mode.

Section 4. Ir L$_{III}$-edge XANES of pristine and cycled SrIrO$_3$
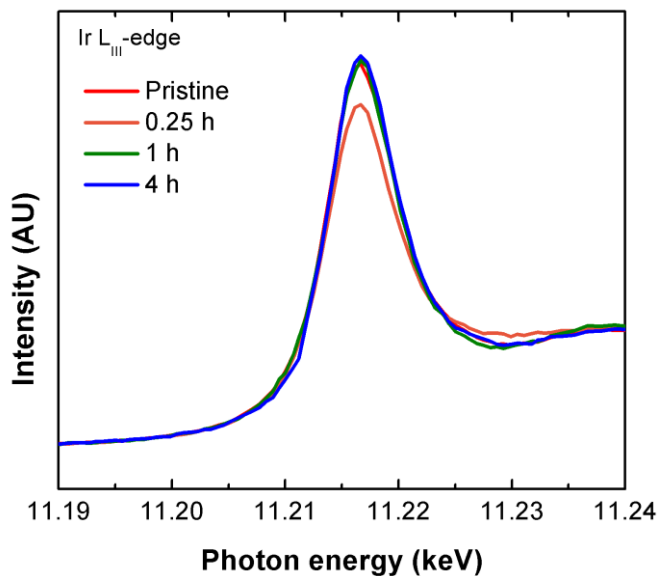
Fig. S7. The bulk sensitive Ir L$_{III}$-edge XANES of pristine SrIrO$_3$, SrIrO$_3$ after 0.25 h, 1h, and 4h of cycling. When an incidence angle of 45° is used, the XANES experiment probes the whole SrIrO$_3$ film. Except at the 0.25 h time point, the bulk average Ir formal oxidation does not change after OER cycling, indicating coupled Sr^{2+} and O^{2-} diffusion, *i.e.,* the loss of Sr and O occurs in a way that preserves the Ir formal oxidation charge.

Section 5. Ir L$_{III}$-edge GI-EXAFS of pristine and cycled SrIrO$_3$
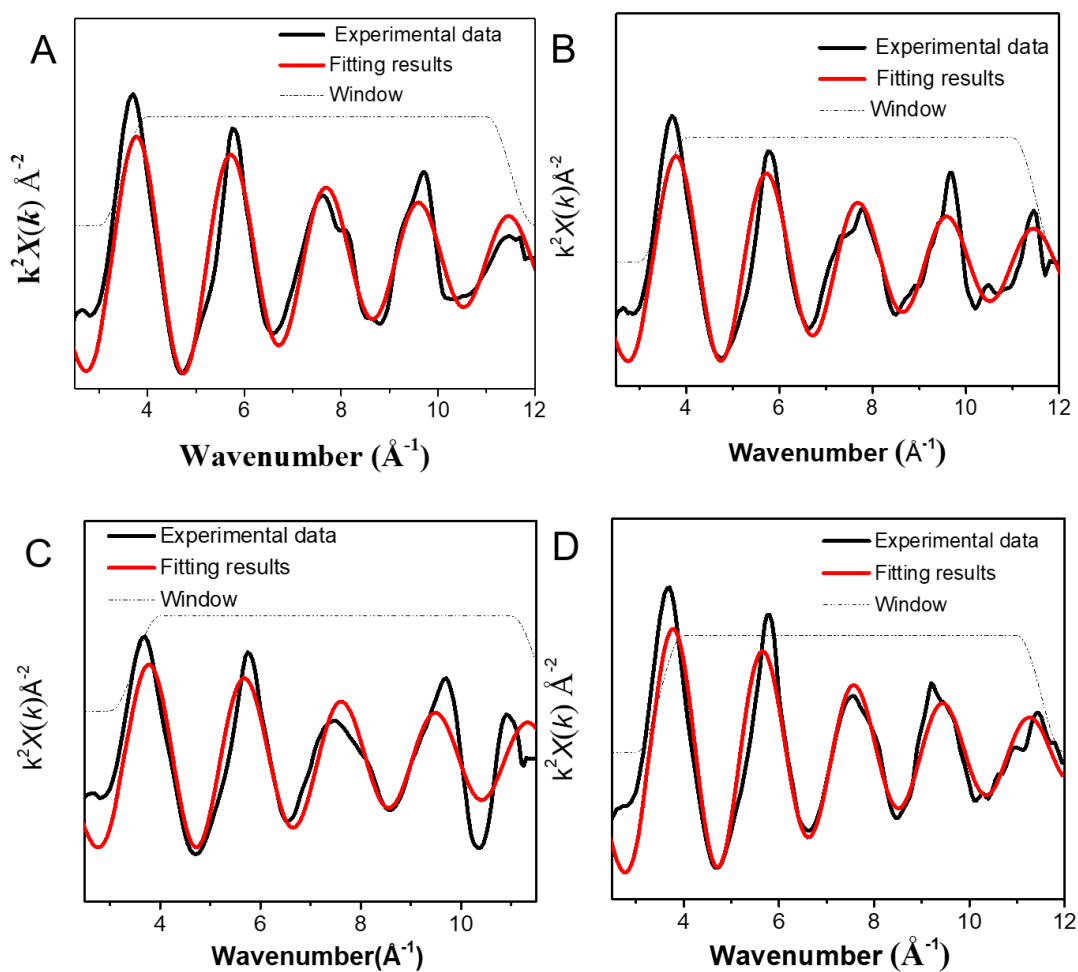
Fig. S8. The *k*-range fitting results of Ir L$_{III}$-edge EXAFS for (A) pristine SrIrO$_3$, (B) SrIrO$_3$ after 0.25 h of cycling, (C) 1h, and (D) 4h. The wavenumber ranged used for fitting is defined by the window curves in all figures.

SrIrO$_3$ Conditions	Shell	CN (error bars)	R (Å)	σ^2 (10^{-4}Å^2)	ΔE (eV)	R factor (%)	K-Range (Å^{-1})	R-Range (Å)
Pristine	Ir-O^1	4 (0.4)	2.007	3.8	11.372	0.6	3.5 -11.5	1.22 - 2.4
	Ir-O^2	2 (0.2)	2.05	3.8	11.372			
0.25h	Ir-O^1	3.0 (0.27)	2.007	7.4	11.981	0.67	3.5-11.5	1.26 - 2.43
	Ir-O^2	1.5 (0.14)	2.05	7.4	11.981			
1h	Ir-O^1	3.5 (0.4)	2.007	3.2	13.246	1.73	3.5 -11.5	1.25-2.2
	Ir-O^2	1.8 (0.2)	2.05	3.2	13.246			
4h	Ir-O^1	3.9 (0.4)	2.007	11.1	13.901	1.94	3.5 -11.5	1.3 - 2.5
	Ir-O^2	1.9 (0.2)	2.05	11.1	13.901			

We determine an S_0^2 value (the amplitude parameter) of 0.84 as the best match for pristine SrIrO$_3$ (using six coordination oxygen atoms around Ir center). We keep this value for the XAFS fit. In the polarization-dependent measurement at the APS 20-ID-C station (for the out-of-plane measurement), four oxygens in the measurement plane gives 100% effective contribution, while the top and bottom O with 90 degree perspective to the centered Ir have zero contribution. This is due to the polarization dependence of the grazing incidence X-ray spectroscopy measurement.

[1] Fitting results from the in-plane Ir-O contribution;
[2] Fitting results from the out-of-plane Ir-O contribution;
The total coordination contains both in-plane and out-of-plane Ir-O.

Table S3. **Structural parameters of SrIrO$_3$ obtained using EXAFS including the Average coordination number (CN), Path Distance (R), Debye−Waller Factor (σ^2), Threshold Energy Correction (ΔE), K-Space Range for Fourier Transform (K-Range) and R-Space Range for Fitting (R-Range), and the R-Factor of the Fitting.**

Section 6. O K-edge NEXAFS of cycled SrIrO$_3$
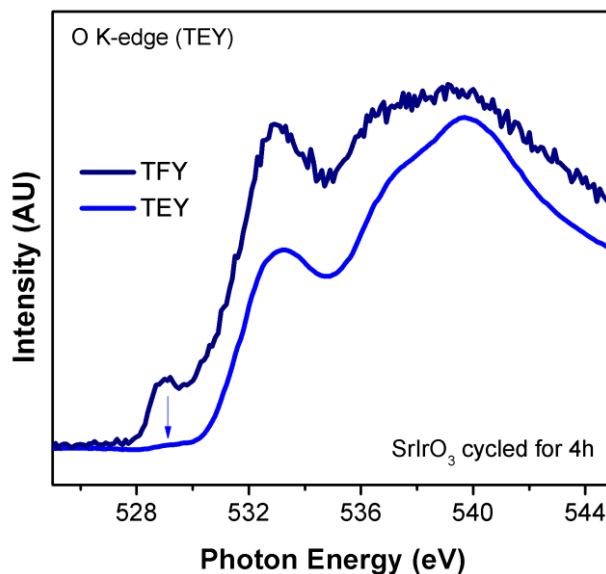
Fig. S9. The O K-edge XANES of SrIrO$_3$ after 4h of cycling via bulk-sensitive TFY and surface-sensitive TEY mode. We observe the reduced pre-edge signal only in the surface-sensitive TEY mode. The O K-edge pre-edge feature contains structural information regarding the amorphous IrO$_x$ layer at the surface.
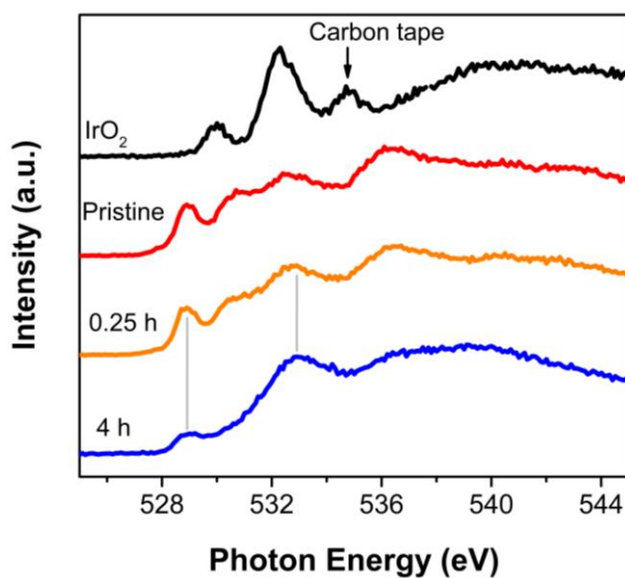

Fig. S10. The O K-edge XANES of IrO$_2$, pristine SrIrO$_3$, and SrIrO$_3$ cycled for 0.25h and 4h in the bulk-sensitive TFY detection mode.

Section 7. First-Principles Calculation Results

## 7.1. Computed dissolution driving force and energy barrier for O and Sr migration

We used DFT-GGA-PBE to evaluate the free energy of dissolution for $SrIrO_3$ through the reaction $SrIrO_3 + 2H^+ \rightarrow IrO_2 + Sr^{2+} + H_2O$. The ion energies have been extracted from experimental data following the approach of Persson et al. (*41*) The computed reaction energy is –2.2 eV at the pH = 0 condition, indicating a strong driving force for dissolution. While this process is favored thermodynamically, the migration energetics of Sr and O displays a varied behavior depending on the amount of oxygen present in the system. To quantify this effect DFT-PBE computations using the climbing image nudge elastic band (CI-NEB) were performed and converged until the total energy change and the forces were less than 10^{-5} eV and 0.05 eV/Å. Different migration paths considered in a pristine $SrIrO_3$ supercell with 160 atoms show very different activation energies for Sr (3.0 eV) and O (1.9 eV). However, the barrier for Sr decreases considerably just by removing one or two of the oxygens around its path (2.7 eV and 2.25 eV, respectively). Inspecting structures with even lower oxygen concentration, in particular the most stable square planar $Sr_{0.5}IrO_2$ structure that was considered in this study (see **Section 7.2** and **Fig. S11**), it was observed that the activation energy for Sr can drop to 1.9 eV, the same value as O in pristine $SrIrO_3$. This further supports the hypotesis that oxygen deficiency strongly faciliates strontium migration.
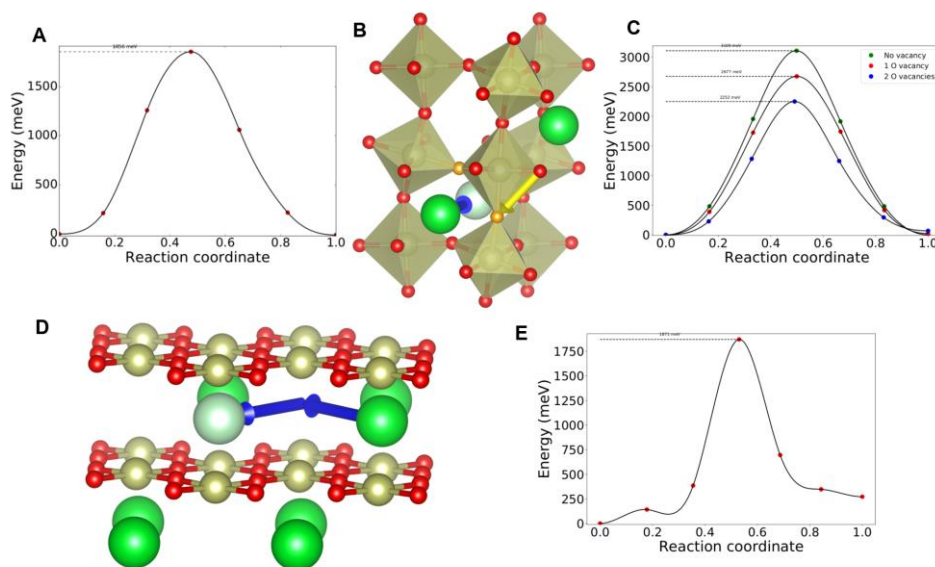
Figure S11. **Graphical representation of the migration paths considered and their barriers, obtained trough CI-NEB simulations.** Green, gold and red spheres represent Sr, Ir and O atoms, respectively. Light green spheres indicate the position of the vacancy where the Sr atoms migrate. Orange atoms in **(B)** identify the oxygen vacancies that are introduced for Sr migration. **(A)** and **(C)** show the migration barrier for O and Sr migration in $SrIrO_3$, respectively. The Sr migration path for the square planar $Sr_{0.5}IrO_2$ structure, depicted in **(D)**, passes through a local minimum. The barrier has been calculated splitting the path in two almost equivalent steps, corresponding to the two blue arrows. **(E)** represents the calculated barrier for the first step.

## 7.2. Evidence for the preference of the square-planar local environment for Ir^{3+}

Starting from the $SrIrO_3$ structure, we have generated a series of structures by removing oxygen and strontium to form $Sr_{0.5}Ir^{3+}O_2$ structures (in order to match the XANES and EXAFS results). The removal of oxygen can lead to a tetrahedral (as in the brownmillerite structures) or square planar (as in square planar $SrFeO_2$) (44) local environment for Ir^{3+} depending on which oxygen atoms are removed. **Fig. S12** shows the generated structures and their energies with respect to the lowest-energy structure. Our computations indicate that the lowest energy structures are the ones forming square planar iridium and that structures with (distorted) tetrahedra are less favorable energetically (over 100 meV/atoms higher in energy).
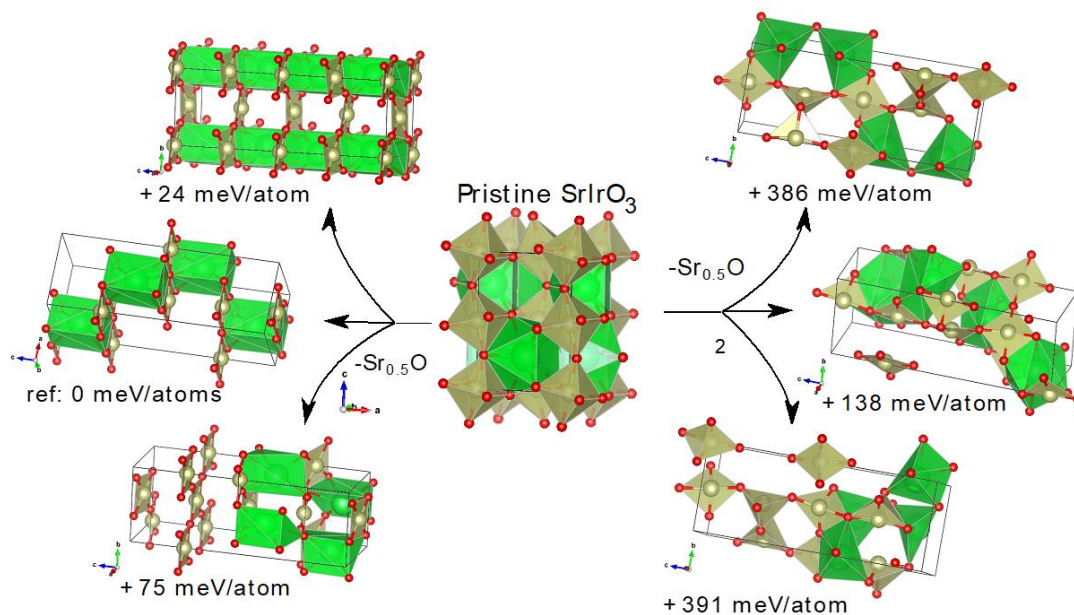
Fig. S12. Tetrahedral and square planar $Sr_{0.5}IrO_2$ structures generated by removing strontium and oxygen from the $SrIrO_3$ perovskite structure. The lowest energy structures were found to be the structure forming square planar iridium.

7.3. IrO₂ polymorphs stability and O K-edge analysis

We computed the energies of various IrO_2 polymorphs using the structure library from 273 MO_x known polymorphs from the Materials Project. We compared the DFT-computed energies to rutile IrO_2. We find the most stable Ir^{4+} polymorphs are the ones containing Ir^{4+} octahedral geometries, with rutile as the lowest-energy structure. **Fig. S13** shows the five lowest energy structures: brookite, hollandite, romanechite, anatase, and rutile. Using the hypothesis that these structures represent the structure of the amorphous IrO_x at the local level, we computed the corresponding O K-edge spectra on each of these IrO_2 structures. We note that we are not seeking perfect agreement with experiment in this calculation, as we are not aiming to solve the structure of the amorphous IrO_x phase. Instead, we look for structural features in the crystalline phases that could lead to similar O K-edge features with the experimental data. We emphasize that the FEFF computations cannot provide reliable absolute energy-value information. We therefore shifted the calculated spectra to match the experiment. All calculated structures show sharp t_{2g}-e_g peaks in their computed O K-edge, in agreement with several prior studies. Interestingly, the romanechite and hollandite show weaker e_g peak signals due to their different oxygen local environments.
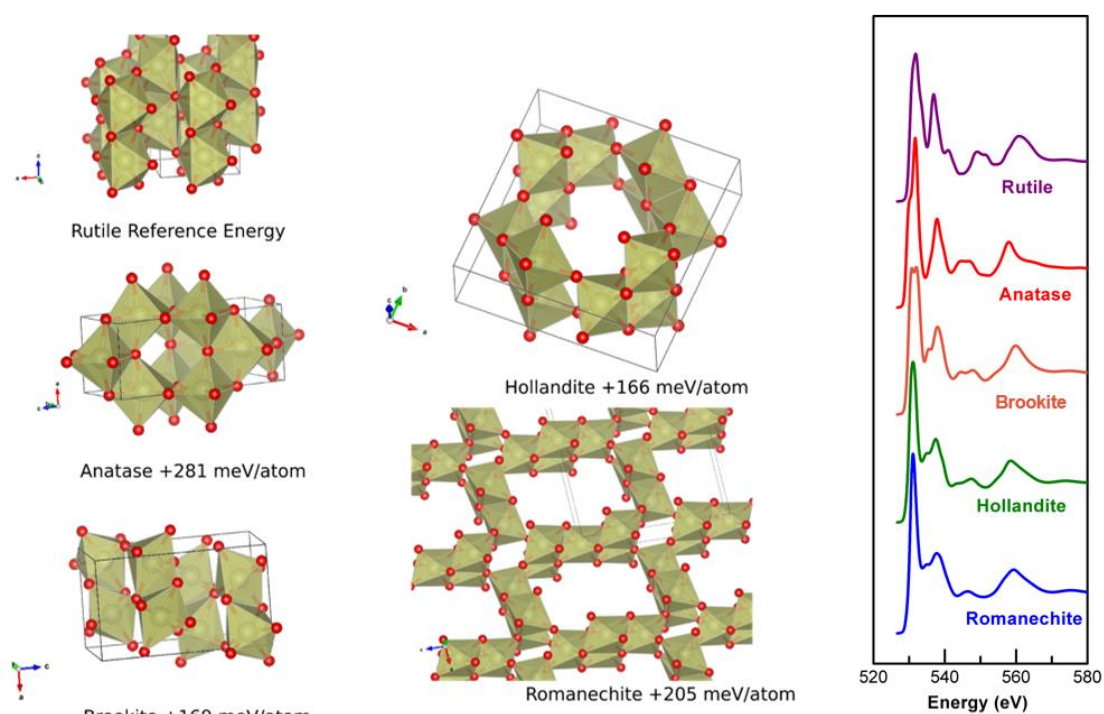
Fig. S13. The five most stable IrO₂ polymorphs with their DFT energy and corresponding simulated O K-edges.

7.4. Amorphous IrO₂ O K-edge

To obtain models of amorphous octahedral IrO_2, we used previously generated TiO_2 amorphous structures (through a "melt and quenching" method) and replaces the Ti by Ir. (*30*) The models were ionically relaxed after the substitution using DFT. Three models of amorphous IrO_2 two with 96 (96-1 and 96-2) and one with 192 atoms were generated. **Fig. S14** show the relaxed structures and their O K-edge spectra**.** We provide the structures as cifs in SI.
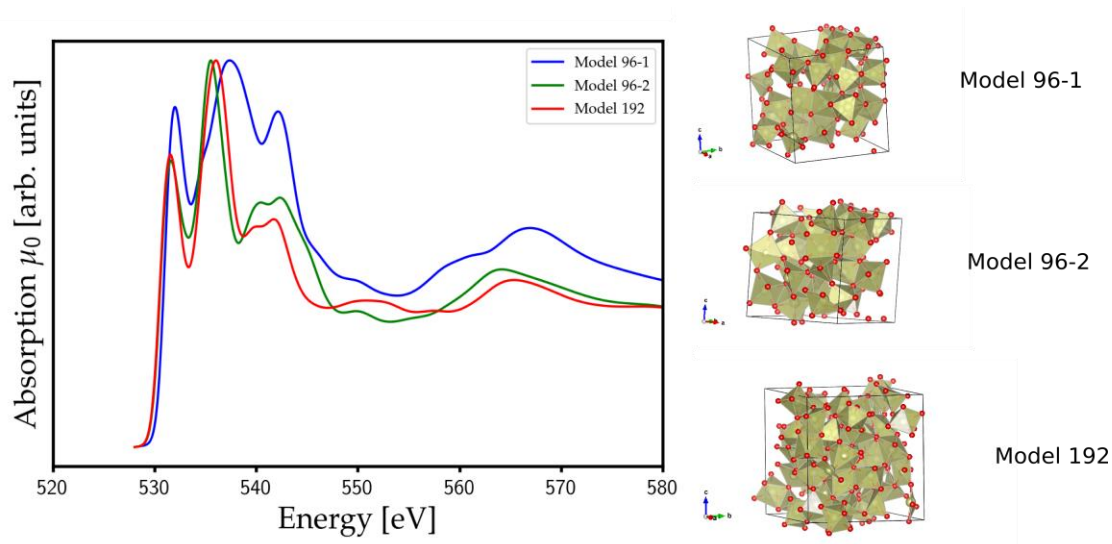
Fig. S14. Amorphous structure models and their computational O K-edge spectra.